

# Recurrent Contour-based Instance Segmentation with Progressive Learning

Hao Feng, Wengang Zhou, Yufei Yin, Jiajun Deng, Qi Sun, and Houqiang Li, *Fellow, IEEE*

**Abstract**—Contour-based instance segmentation has been actively studied, thanks to its flexibility and elegance in processing visual objects within complex backgrounds. In this work, we propose a novel deep network architecture, *i.e.*, PolySnake, for contour-based instance segmentation. Motivated by the classic Snake algorithm, the proposed PolySnake achieves superior and robust segmentation performance with an iterative and progressive contour refinement strategy. Technically, PolySnake introduces a recurrent update operator to estimate the object contour iteratively. It maintains a single estimate of the contour that is progressively deformed toward the object boundary. At each iteration, PolySnake builds a semantic-rich representation for the current contour and feeds it to the recurrent operator for further contour adjustment. Through the iterative refinements, the contour finally progressively converges to a stable status that tightly encloses the object instance. Moreover, with a compact design of the recurrent architecture, we ensure the running efficiency under multiple iterations. Extensive experiments are conducted to validate the merits of our method, and the results demonstrate that the proposed PolySnake outperforms the existing contour-based instance segmentation methods on several prevalent instance segmentation benchmarks. The codes and models are available at <https://github.com/fh2019ustc/PolySnake>.

**Index Terms**—Contour-based, Instance Segmentation, Progressive Learning, Recurrent Architecture

## 1 INTRODUCTION

Instance segmentation is a fundamental computer vision task, aiming to recognize each distinct object in an image along with their associated outlines. The advance of instance segmentation benefits a broad range of visual understanding applications, such as autonomous driving [1], [2], augmented reality [3], [4], robotic grasping [5], [6], surface defect detection [7], [8], and so on. Over the past few years, instance segmentation has been receiving increased attention and significant progress has been made.

In the literature, most of the state-of-the-art methods [9], [10], [11], [12], [13], [14], [15], [16], [17] adopt a two-stage pipeline for instance segmentation. Typically, they first detect the object instance in the form of bounding boxes (see Fig. 1(b)) and then estimate a pixel-wise segmentation mask (see Fig. 1(c)) within each bounding box. However, the segmentation performance of such methods is limited due to the inaccurate bounding boxes. For example, the classic Mask R-CNN [9] performs a binary classification on a  $28 \times 28$  feature map of a detected instance. Besides, their dense prediction architecture usually suffers from heavy computational overhead [18], limiting their applications in resource-limited scenarios with a real-time requirement.

To address the above issues, recent research efforts have been dedicated to designing alternative representations to the pixel-wise segmentation mask. One kind of intuitive representative scheme is the object contour, in the form of a sequence of vertexes along the object silhouette (see Fig. 1(d)). Typically, PolarMask [19], [20] innovatively applies the angle and distance terms in a polar

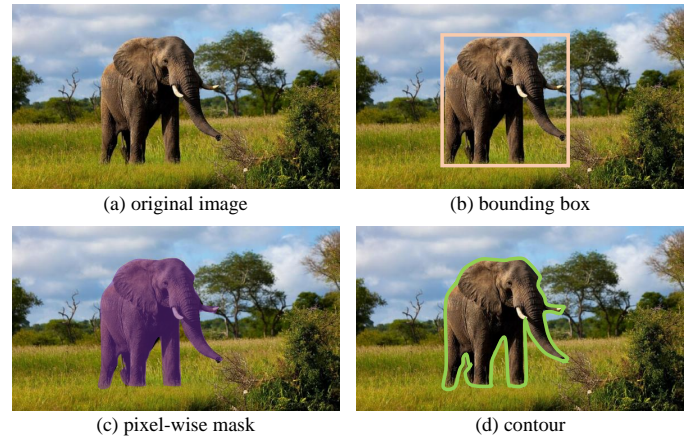


Fig. 1. An illustration of different representations to localize an instance in an image: (b) bounding box, (c) pixel-wise mask, and (d) contour.

coordinate system to localize the vertices of the contour, which achieves competitive accuracy. However, in PolarMask [19], [20], contours are constructed from a set of endpoints of concentric rays emitted from the object center, thus restricting the models to handling convex shapes as well as some concave shapes with non-intersecting rays. Another pioneering method is DeepSnake [21] which directly regresses the coordinates of contour vertexes in the Cartesian coordinate system. Inspired by the classic Snake algorithm [22], DeepSnake [21] devises a neural network to evolve an initial contour to enclose the object boundary. Based on this strong baseline, other methods [23], [24], [25], [26], [27], [28] continue to explore a more effective contour estimation strategy. Among them, Curve-GCN [26] introduces Graph Convolutional Network (GCN) [29] for contour estimation. However, it needs an extra manual annotation of the object. Dance [27] proposes an effective segment-wise matching mechanism to build the ground truth contour (a sequence of vertex). E2EC [28] applies a novel

- Hao Feng, Wengang Zhou, Yufei Yin, Qi Sun and Houqiang Li are with the CAS Key Laboratory of Technology in Geo-spatial Information Processing and Application System, Department of Electronic Engineering and Information Science, University of Science and Technology of China, Hefei, 230027, China. E-mail: {fh1995,yinyufei,sq008}@mail.ustc.edu.cn; {zhwg,lihq}@ustc.edu.cn.
- Jiajun Deng is with The University of Sydney, NSW, 2006, Australia. E-mail: jiajun.deng@sydney.edu.au.
- Corresponding authors: Wengang Zhou and Houqiang Li.

learnable contour initialization architecture and global contour deformation module. Although they report promising performance on the challenging benchmarks [30], [31], [32], [33], their contour learning strategies are somewhat heuristic and complex.

In this paper, we propose PolySnake, a new deep network architecture for contour-based instance segmentation. The idea of our PolySnake is traced back to the classic Snake algorithm [22] that iteratively deforms an initial polygon to progressively match the object boundary by the optimization of an energy function. Correspondingly, PolySnake also aims to realize effective automatic contour learning based on iterative and progressive mechanisms simultaneously, different from existing methods. Specifically, given an initial contour of an object instance, PolySnake develops a recurrent update operator to estimate the contour iteratively. It maintains a single estimate of the contour that is progressively deformed at each iteration. At each iteration, PolySnake first constructs the representation of the contour estimated at the previous iteration. Then, the recurrent operator takes the features as input and estimates the residual displacement to adjust the current coarse contour to further outline the object instance. Through the iterative refinements, the contour finally progressively converges to a stable status that tightly encloses the object instance. Note that in the existing methods [21], [27], [28], the contour deformation modules are simply stacked, to include more times of refinement. Nevertheless, the overlarge model size increases the learning difficulty and thus harms the performance. Typically, the performance of DeepSnake [21] drops with more than 4 times contour adjustment.

Additionally, our PolySnake exhibits a novel design in three aspects. Firstly, PolySnake takes a neat network architecture. Due to its recurrent design, the whole model is still lightweight, free from the iteration times. Moreover, the lightweight architecture also ensures the real-time ability even under a relatively large number of iterations. Secondly, to achieve a high-quality estimation, we present a multi-scale contour refinement module to further refine the obtained contour with a fine-grained but semantic-rich feature map. Thirdly, we propose a shape loss to encourage and regularize the learning of object shape, which makes the regressed contour outline the object instance more tightly.

To evaluate the effectiveness of our PolySnake, we conduct comprehensive experiments on several prevalent instance segmentation benchmark datasets, including SBD [30], Cityscapes [31], COCO [32], and KINS [33]. Extensive quantitative and qualitative results demonstrate the merits of our method as well as its superiority over state-of-the-art methods. Moreover, we validate various design choices of PolySnake through comprehensive studies.

## 2 RELATED WORK

We broadly categorize the research on instance segmentation into three directions, including mask-based, contour-based, and other methods. In the following, we discuss them separately.

### 2.1 Mask-based Instance Segmentation

Most recent works perform instance segmentation by predicting pixel-level masks. Some of these works follow the paradigm of ‘‘Detect then Segment’’ [9], [10], [11], [12], [13], [14], [15], [16], [34]. They usually first detect the bounding boxes and then predict foreground masks in the region of each bounding box. Among them, the classic Mask R-CNN [9] supplements a segmentation branch on Faster R-CNN [35] for per-pixel binary classification

in each region proposal. To enhance the feature representation, PANet [12] proposes bottom-up path augmentation to enhance information propagation based on Mask R-CNN [9], and A<sup>2</sup>-FPN [15] strengthens pyramidal feature representations through attention-guided feature aggregation. To improve the segmentation parts, Mask Scoring R-CNN [11] adds a MaskIoU head to learn the completeness of the predicted masks. HTC [10] and RefineMask [14] integrate cascade into instance segmentation by interweaving detection and segmentation features [10] or fusing the instance features obtained from different stages [14]. Recently, DCT-Mask [13] introduces DCT mask representation to reduce the complexity of mask representation, and BPR [16] proposes the crop-then-refine strategy to improve the boundary quality.

There also exist some works that are free of bounding boxes. YOLACT [36] generates several prototype masks over the entire image and predicts a set of coefficients for each instance to combine them. BlendMask [37] directly predicts 2D attention map for each proposal on the top of the FCOS detector [38], and combines them with ROI features. Besides, recent attempts [39], [40], [41], [42] have also applied dynamic convolution kernels trained online, which are then performed on feature maps to generate instance masks.

### 2.2 Contour-based Instance Segmentation

Contour-based methods aim to predict a sequence of vertices of object boundaries, which are usually more lightweight than pixel-based methods. Some methods [19], [20], [24] use polar-representation to predict contours directly. Among them, PolarMask [19], [20] extends classic detection algorithm FCOS [38] to instance segmentation, which adds an additional regression head to predict distances from the center point to each boundary vertex. However, performances of such methods are usually limited when dealing with objects with some complex concave shapes. ESE-Seg [24] utilizes Chebyshev polynomials [43] to approximate the shape vector and adds an extra branch on YOLOv3 [44] to regress the coefficients of Chebyshev polynomials.

Some other works [21], [25], [27], [28], [45] apply Cartesian coordinate representation for vertices, and regress them towards ground-truth object boundaries. Typically, DeepSnake [21] first initializes the contours based on the box predictions, and then applies several contour deformation steps for segmentation. Based on DeepSnake [21], Dance [27] improves the matching scheme between predicted and target contours and introduces an attentive deformation mechanism. ContourRender [45] uses DCT coordinate signature and applies a differentiable renderer to render the contour mesh. Eigencontours [46] proposes a contour descriptor based on low-rank approximation and then incorporates the eigencontours into an instance segmentation framework. Recently, E2EC [28] applies a novel learnable contour initialization architecture and shows remarkable performance.

Different from the above works, our PolySnake introduces an iterative and progressive mechanism into the learning of object contour, achieving superior and robust contour estimation.

### 2.3 Other Instance Segmentation Methods

Dense RepPoints [47] uses a set of adaptive sparse points to represent an object segment, but this representation needs complex post-processing steps to be converted into binary masks. PolyTransform [25] segments individual objects first and then converts the generated masks into the initial contours [48]. The contours

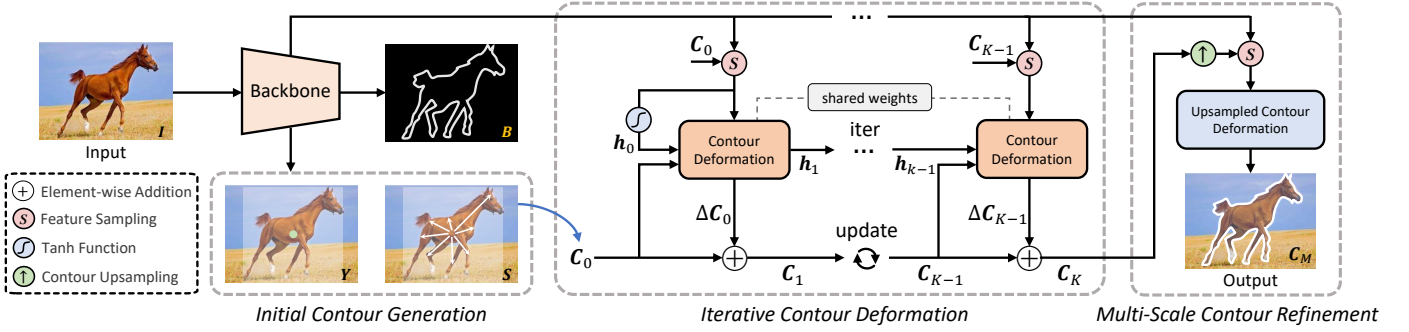


Fig. 2. An overview of the proposed PolySnake framework. PolySnake consists of three modules: Initial Contour Generation (ICG), Iterative Contour Deformation (ICD), and Multi-scale Contour Refinement (MCR). Given an input image  $I$ , ICG first initializes a coarse contour  $C_0$  based on the predicted center heatmap  $Y$  and offset map  $S$ . Then, in ICD, the obtained contour  $C_0$  is progressively deformed with  $K$  iterations. After that, in MCR, we construct a large-scale but semantic-rich feature map for a further refinement and obtain the output contour  $C_M$ .

are then fed to a deforming network [49] that transforms the polygons such that they better enclose the objects. BoxInst [50] achieves mask-level instance segmentation with only bounding-box annotations by redesigning the loss of learning masks.

### 3 METHODOLOGY

An overview of the proposed PolySnake is shown in Fig. 2. Similar to the classic Snake algorithm [22], PolySnake iteratively deforms the contours to progressively match the object boundary. We first develop a recurrent architecture that allows a single estimate of the contour progressively updated at each iteration, and further refine the obtained contour at original image scale. Through iterative refinements, the contours progressively enclose the object and finally converge to a relatively steady status. For the convenience of understanding, we divide the framework into three modules, including (1) initial contour generation, (2) iterative contour deformation, and (3) multi-scale contour refinement. In the following, we separately elaborate them.

#### 3.1 Initial Contour Generation

The **Initial Contour Generation (ICG)** module aims to construct an initial contour for an object instance. Based on CenterNet [51], both DeepSnake [21] and Dance [27] initialize a contour from the detected bounding box with a rectangle, while E2EC [28] directly regresses an ordered vertex set as the initial contour. In our PolySnake, we initialize the coarse contours based on the basic setting of E2EC [28], described next.

Specifically, given an input RGB image  $I \in \mathbb{R}^{H \times W \times 3}$  with width  $W$  and height  $H$ , we first inject it to a backbone network [52], and obtain a feature map  $F \in \mathbb{R}^{\frac{H}{R} \times \frac{W}{R} \times D}$ , where  $R = 4$  is the output stride and  $D$  denotes the channel number. Then, as shown in Fig. 2, the initial contour is generated with three parallel branches. The first branch predicts a center heatmap  $Y \in [0, 1]^{\frac{H}{R} \times \frac{W}{R} \times C}$ , where  $C$  is the number of object categories. The second branch regresses an offset map  $S \in \mathbb{R}^{\frac{H}{R} \times \frac{W}{R} \times 2N_v}$ , where  $N_v$  denotes the vertex number to form an object contour. Let  $(x_i, y_j)$  denote the center coordinate of an object, then its contour can be obtained by adding the predicted offset  $\{(\Delta x^k, \Delta y^k) | k = 1, 2, \dots, N_v\}$  at  $(x_i, y_j)$  of  $S$ . Moreover, we supplement an extra branch. It predicts a category-agnostic boundary map  $B \in \mathbb{R}^{\frac{H}{R} \times \frac{W}{R}}$ , in which each value is a classification confidence (boundary/non-boundary). Our motivation is that such

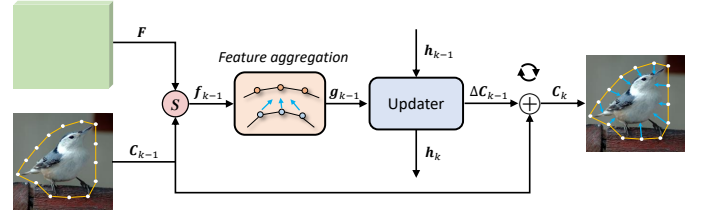


Fig. 3. An illustration of the  $k^{th}$  iteration in the ICD module. “S” denotes vertex feature sampling based on bilinear interpolation. “+” represents element-wise addition for deforming the current contour.

a branch can help to extract the more fine-grained features for the perception of object boundaries. Note that this branch is only used in the training, which will not cause an extra computation burden for inference. During inference, the instance center can be obtained efficiently based on the max pooling operation [51] on the heatmap  $Y$ . Finally, we obtain the initial contour  $C_0 \in \mathbb{R}^{N_v \times 2}$  used for the following refinements.

#### 3.2 Iterative Contour Deformation

Given the initial contour of an object instance, the **Iterative Contour Deformation (ICD)** module maintains a single estimation of object contour, which is refined iteratively. In this way, the initial contour finally converges to a stable state tightly enclosing the object. The architecture of the ICD module is neat, which contributes to the low latency of our method even with a relatively large number of iterations.

The workflow of ICD module is illustrated in Fig. 2. Given the feature map  $F \in \mathbb{R}^{\frac{H}{R} \times \frac{W}{R} \times D}$  extracted by the backbone network and the initial contour  $C_0 = \{p_0^1, p_0^2, \dots, p_0^{N_v}\} \in \mathbb{R}^{N_v \times 2}$  of an object, we deform the object contour iteratively and output the sequence  $\{C_1, C_2, \dots, C_K\}$ , where  $C_k = \{p_k^1, p_k^2, \dots, p_k^{N_v}\}$  is the predicted object contour with  $N_v$  vertices at the  $k^{th}$  iteration, and  $K$  is the total iteration number. Note that the two channels of the contour  $C_k \in \mathbb{R}^{N_v \times 2}$  denote the horizontal and the vertical coordinates of  $N_v$  vertices, respectively. After  $K$  iterations, we produce the high-quality object contour  $C_K$ .

As shown in Fig. 3, we illustrate the contour update process at the  $k^{th}$  iteration. Given the feature map  $F \in \mathbb{R}^{\frac{H}{R} \times \frac{W}{R} \times D}$  and the contour  $C_{k-1}$  predicted at the  $(k-1)^{th}$  iteration, we first sample the vertex-wise feature and then aggregate them for deforming the current contour. We divide the contour update process in ICD module into three sub-processes, including (1) vertex feature

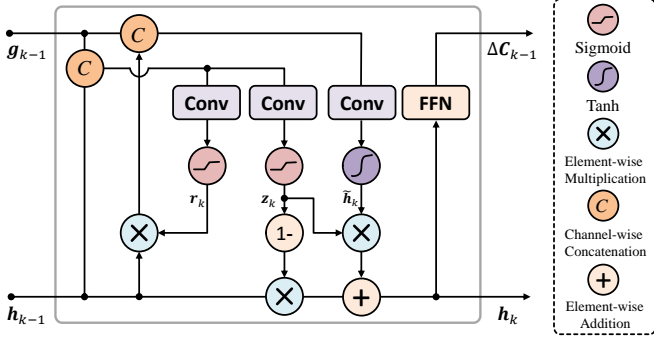


Fig. 4. Inner structure of the GRU-based vertex coordinate updater.

sampling, (2) vertex feature aggregation, and (3) vertex coordinate update, as described in the following.

**Vertex feature sampling.** Given the feature map  $F \in \mathbb{R}^{\frac{H}{R} \times \frac{W}{R} \times D}$  and the contour  $C_{k-1} \in \mathbb{R}^{N_v \times 2}$  with  $N_v$  vertices  $\{\mathbf{p}_{k-1}^1, \mathbf{p}_{k-1}^2, \dots, \mathbf{p}_{k-1}^{N_v}\}$  predicted at the  $(k-1)^{th}$  iteration, we first retrieve features of these  $N_v$  vertices. Specifically, given a vertex  $\mathbf{p}_{k-1}^i \in \mathbb{R}^2$ , we sample its feature vector  $F(\mathbf{p}_{k-1}^i) \in \mathbb{R}^D$  on the feature map  $F$  based on the bilinear interpolation. Note that according to classic STN [53], we can compute the gradients to the input  $F$  and  $C_{k-1}$  for backpropagation, thus the module can be trained in an end-to-end manner. After that, we concatenate the feature vectors of the total  $N_v$  vertices and produce the vertex feature  $\mathbf{f}_{k-1} \in \mathbb{R}^{N_v \times D}$  at the  $(k-1)^{th}$  iteration.

**Vertex feature aggregation.** This module constructs the contour-level representation for  $C_{k-1}$  by fusing the vertex features  $\mathbf{f}_{k-1}$ . Following [21], [27], [28], [54], we use the circle-convolution to fuse the feature of the contour. The circle-convolution operation firstly joins up the head and tail of the input sequence and then applies a standard 1-D convolution on it, which is applicable to capture features of a contour with a polygon topology. In our implementation, we first stack eight circle-convolution layers with residual skip connections for all the layers. Then, we concatenate the features from all the layers and forward them through three  $1 \times 1$  convolutional layers. Finally, we explicitly concatenate the output features with contour coordinate  $C_{k-1} \in \mathbb{R}^{N_v \times 2}$ , obtaining the contour representation  $\mathbf{g}_{k-1} \in \mathbb{R}^{N_v \times D_v}$ .

**Vertex coordinate update.** To make the contour enclose the object tightly, we introduce a recurrent update operator that iteratively updates the currently estimated contour. Fig. 4 illustrates the structure of our GRU-based update operator. It is a gated activation unit based on the GRU cell [55], in which the fully connected layers are replaced with the 1-D convolutional layers. At the  $k^{th}$  iteration, it takes the contour representation  $\mathbf{g}_{k-1} \in \mathbb{R}^{N_v \times D_v}$  as well as the hidden state  $\mathbf{h}_{k-1} \in \mathbb{R}^{N_v \times D_v}$  as input, differentiates them, and outputs the hidden states  $\mathbf{h}_k \in \mathbb{R}^{N_v \times D_v}$  as follows,

$$\mathbf{z}_k = \sigma(\text{Conv}([\mathbf{h}_{k-1}, \mathbf{g}_{k-1}], \mathbf{W}_z)), \quad (1)$$

$$\mathbf{r}_k = \sigma(\text{Conv}([\mathbf{h}_{k-1}, \mathbf{g}_{k-1}], \mathbf{W}_r)), \quad (2)$$

$$\tilde{\mathbf{h}}_k = \tanh(\text{Conv}([\mathbf{r}_k \odot \mathbf{h}_{k-1}, \mathbf{g}_{k-1}], \mathbf{W}_h)), \quad (3)$$

$$\mathbf{h}_k = (1 - \mathbf{z}_k) \odot \mathbf{h}_{k-1} + \mathbf{z}_k \odot \tilde{\mathbf{h}}_k, \quad (4)$$

where  $\odot$  denotes element-wise multiplication;  $\mathbf{W}_z$ ,  $\mathbf{W}_r$ , and  $\mathbf{W}_h$  are the weights for the corresponding gates. Note that the initial hidden state  $\mathbf{h}_0$  is initialized as the contour feature  $\mathbf{g}_0 \in \mathbb{R}^{N_v \times D_v}$  that is processed by the  $\tanh$  activation function.

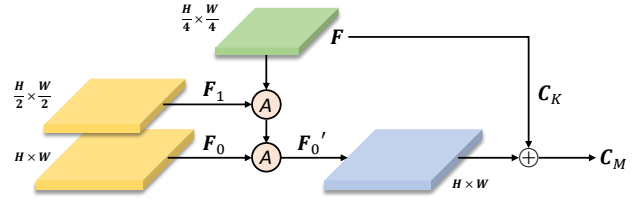


Fig. 5. An overview of the multi-scale contour refinement module. “A” denotes the feature fusion process, following FPN [56].

After that, two convolutional layers with a ReLU activation follow  $\mathbf{h}_k \in \mathbb{R}^{N_v \times D_v}$  to produce the residual displacement  $\Delta C_{k-1} \in \mathbb{R}^{N_v \times 2}$ , which is used to update the coordinate of current contour  $C_{k-1}$  as follows,

$$C_k = C_{k-1} + \Delta C_{k-1}. \quad (5)$$

After  $K$  iterations, we obtain the contour prediction  $C_K \in \mathbb{R}^{N_v \times 2}$  tightly enclosing the object instance, as shown in Fig. 2.

### 3.3 Multi-scale Contour Refinement

The output contour  $C_K$  is obtained based on the retrieved contour feature from the  $\frac{1}{R}$  scale feature map  $F \in \mathbb{R}^{\frac{H}{R} \times \frac{W}{R} \times D}$ . Note that we set  $R = 4$  by default, following DeepSnake [21] and E2EC [28]. However, the feature map  $F$  is semantically strong, but the high-frequency features on object boundaries are inadequate after all the downsampling and upsampling operations in the network, which brings difficulties to localize the object contours. To this end, MCR module is proposed to further refine the obtained  $C_K$  with a large-scale but semantic-rich feature map.

Specifically, we first take two additional low-level large-scale feature maps from the backbone network (*i.e.*,  $F_0 \in \mathbb{R}^{H \times W \times D_0}$  and  $F_1 \in \mathbb{R}^{\frac{H}{2} \times \frac{W}{2} \times D_1}$ ). Note that the high-frequency signals are reserved in  $F_0$  and  $F_1$ . Then, as shown in Fig. 5, to aggregate with the semantically stronger feature map  $F$ , we build a simple feature pyramid network [56] to construct feature map  $F_0' \in \mathbb{R}^{H \times W \times D_2}$  used for following contour refinement.

Based on the feature map  $F_0'$ , we further deform  $C_K$  toward the object boundary. The contour deformation process is similar to that in the ICD module, except that the GRU-based recurrent update operator is removed. Concretely, given the feature map  $F_0'$  and the current contour  $C_K$ , we sample the per-vertex feature, aggregate them, and directly predict per-vertex offset to update the contour with a fully connected layer. Finally, we obtain the refined contour estimation, termed as  $C_M \in \mathbb{R}^{N_v \times 2}$ .

### 3.4 Training Objectives

The training is divided into two stages. Concretely, the ICG and ICD modules are first optimized with the objective as follows,

$$\mathcal{L} = \mathcal{L}_{\text{ICG}} + \mathcal{L}_{\text{ICD}}. \quad (6)$$

Then, we freeze the models and optimize the MCR module with objective  $\mathcal{L}_{\text{MCR}}$ . In the following, we separately elaborate them.

(1)  $\mathcal{L}_{\text{ICG}}$  consists of three terms as follows,

$$\mathcal{L}_{\text{ICG}} = \mathcal{L}_Y + \mathcal{L}_S + \mathcal{L}_B, \quad (7)$$

where  $\mathcal{L}_Y$  and  $\mathcal{L}_S$  are the loss on the predicted center heatmap  $Y$  and offset map  $S$ . We follow the classic detector CenterNet [51] to compute  $\mathcal{L}_Y$  and  $\mathcal{L}_S$  by only changing the output size of the

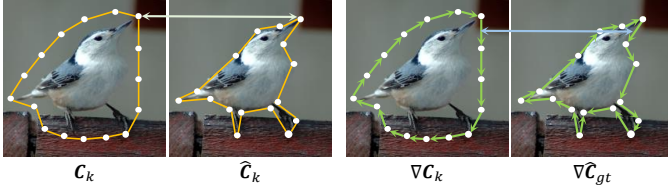


Fig. 6. An illustration of the coordinate regression loss  $\mathcal{L}_R^{(k)}$  (left) and the proposed shape loss  $\mathcal{L}_P^{(k)}$  (right). The loss  $\mathcal{L}_R^{(k)}$  measure the coordinate distance between the predicted contour  $C_k$  and GT contour  $\hat{C}_{gt}$ , while  $\mathcal{L}_P^{(k)}$  encourages the learning of object shape.

offset map  $\mathbf{S}$  from  $\frac{H}{R} \times \frac{W}{R} \times 2N_v$  to  $\frac{H}{R} \times \frac{W}{R} \times 2$  to directly regress the initial contour with  $N_v$  vertices. Besides,  $\mathcal{L}_S$  is the cross-entropy loss between the predicted boundary map  $\mathbf{B}$  and its given ground truth  $\hat{\mathbf{B}}$  as follows,

$$\mathcal{L}_B = - \sum_{i=1}^{N_p} [\hat{y}_i \log(y_i) + (1 - \hat{y}_i) \log(1 - y_i)], \quad (8)$$

where  $N_p = \frac{H}{4} \times \frac{W}{4}$  is the number of pixels in map  $\mathbf{B}$ ,  $\hat{y}_i \in [0, 1]$  and  $y_i \in \{0, 1\}$  denote the ground-truth and the predicted confidence score in  $\hat{\mathbf{B}}$  and  $\mathbf{B}$ , respectively.

(2)  $\mathcal{L}_{ICD}$  is calculated by accumulating the loss over all  $K$  iterations as follows,

$$\mathcal{L}_{ICD} = \sum_{k=1}^K \lambda^{K-k} (\mathcal{L}_R^{(k)} + \alpha \mathcal{L}_P^{(k)}), \quad (9)$$

where  $\mathcal{L}_R^{(k)}$  and  $\mathcal{L}_P^{(k)}$  are the coordinate regression loss and our proposed contour shape loss at the  $k^{th}$  iteration,  $\lambda$  is the temporal weighting factor, and  $\alpha$  is the weight of contour shape loss. Here  $\lambda$  is less than 1, which means the weight of the loss increases exponentially with the iteration. In Fig. 6, we illustrate the coordinate regression loss  $\mathcal{L}_R^{(k)}$  (left) and the proposed shape loss  $\mathcal{L}_P^{(k)}$  (right). Specifically, we compute the coordinate regression loss by calculating the smooth  $L_1$  distance [35] between the predicted contour  $C_k = \{p_k^1, p_k^2, \dots, p_k^{N_v}\}$  and the ground truth  $\hat{C}_{gt} = \{\hat{p}^1, \hat{p}^2, \dots, \hat{p}^{N_v}\}$  as follows,

$$\mathcal{L}_R^{(k)} = \sum_{n=1}^{N_v} \text{smooth}_{L_1}(p_k^n, \hat{p}^n). \quad (10)$$

Furthermore, we denote the offsets of adjacent points in each contour  $\nabla C_k = \{\Delta p_k^{2 \rightarrow 1}, \Delta p_k^{3 \rightarrow 2}, \dots, \Delta p_k^{N_v \rightarrow N_v-1}, \Delta p_k^{1 \rightarrow N_v}\}$  as the shape representation of contour  $C_k$ . Note that since the contour is a closed polygon, the offset between the first and the last points is included in  $\nabla C_k$ . Then, the proposed shape loss  $\mathcal{L}_P^{(k)}$  is defined as the smooth  $L_1$  distance [35] between  $\nabla C_k$  and the ground truth shape representation  $\nabla \hat{C}_{gt}$ , computed as follows,

$$\mathcal{L}_P^{(k)} = \sum_{n=1}^{N_v} \text{smooth}_{L_1}(\Delta p_k^{n+1 \rightarrow n}, \Delta \hat{p}^{n+1 \rightarrow n}). \quad (11)$$

The shape loss encourages the learning of object shape and makes the regressed contour enclose the object tightly.

(3)  $\mathcal{L}_{MCR}$  is calculated as the smooth  $L_1$  distance [35] between the refined contour  $C_M = \{p_M^1, p_M^2, \dots, p_M^{N_v}\}$  and its given ground truth  $\hat{C}_{gt}$  as follows,

$$\mathcal{L}_{MCR} = \sum_{n=1}^{N_v} \text{smooth}_{L_1}(p_M^n, \hat{p}^n). \quad (12)$$

TABLE 1  
Ablations of the initial contour generation module on the SBD val set [30].  $C_0$  and  $C_K$  are the output contour of the ICG and ICD modules, respectively. Settings used in our final model are underlined.

Experiment	Contour	Method	$AP_{vol}$	$AP_{50}$	$AP_{70}$
Boundary Map	$C_0$	w/	<b>49.5</b>	<b>61.2</b>	31.9
		w/o	49.3	61.0	<b>32.2</b>
	$C_K$	w/	<b>59.7</b>	<b>66.7</b>	<b>54.8</b>
		w/o	59.3	66.6	54.4
Vertex Number	$C_K$	$N = 64$	58.9	66.0	54.1
		<u><math>N = 128</math></u>	<b>59.7</b>	<b>66.7</b>	<b>54.8</b>
		$N = 192$	59.2	66.2	54.3

TABLE 2  
Ablations of the iterative contour deformation module on the SBD val set [30]. Settings used in our final model are underlined.

Experiment	Method	$AP_{vol}$	$AP_{50}$	$AP_{70}$	Para. (M)	FPS
Contour Feature	$f_k$	58.6	65.7	53.2	20.3	44.2
	<u><math>g_k</math></u>	<b>59.7</b>	<b>66.7</b>	<b>54.8</b>	22.0	28.8
Update Unit	<u>ConvGRU</u>	<b>59.7</b>	<b>66.7</b>	<b>54.8</b>	22.0	28.8
	ConvLSTM	59.5	66.4	54.6	22.1	24.4
Shared Weights	w/	<b>59.7</b>	<b>66.7</b>	54.8	22.0	-
	w/o	59.6	66.5	<b>55.1</b>	31.0	-
Supervised iters	<u>[1, K]</u>	<b>59.7</b>	<b>66.7</b>	<b>54.8</b>	22.0	-
	$\{K\}$	58.8	66.2	54.0	22.0	-
Shape Loss	w/	<b>59.7</b>	<b>66.7</b>	<b>54.8</b>	-	-
	w/o	59.4	66.2	<b>54.8</b>	-	-

## 4 EXPERIMENTS

### 4.1 Datasets and Metrics

Extensive experiments are conducted on the three widely used datasets for instance segmentation, described next.

**SBD** [30] dataset contains 5623 training and 5732 testing images with 20 semantic categories. It adopts images from the PASCAL VOC [57] dataset, but re-annotates them with instance-level boundaries. For SBD, we report the performance of prior works and our PolySnake based on the metrics 2010 VOC  $AP_{vol}$  [58],  $AP_{50}$ , and  $AP_{70}$ .  $AP_{vol}$  is computed as the average of average precision (AP) with nine thresholds from 0.1 to 0.9.

**Cityscapes** [31] dataset is intended for assessing the performance of vision algorithms of semantic urban scene understanding. The dataset contains 5000 images with high-quality annotations of 8 semantic categories. They are further split into 2975, 500, and 1525 images for training, validation, and testing, respectively. Results are evaluated in terms of the AP metric averaged over all categories of the dataset.

**KINS** [33] dataset is used for amodal instance segmentation [59], which adopts images from the KITTI [60] dataset and annotates them with instance-level semantic annotation. The dataset contains 7474 training and 7517 testing images. We evaluate our approach on seven object categories with the AP metric.

**COCO** [32] dataset is a challenging large-scale dataset for instance segmentation, which contains 115k training, 5k validation, and 20k testing images with 80 object categories. The images in COCO contain everyday objects and humans. We apply the COCO average precision (AP) to evaluate our method.

TABLE 3

Performance of the selected iterations during inference on the SBD val set [30].  $C_0$  is output initial contour of the ICG module. The running efficiency is evaluated on a single RTX 2080Ti GPU. The contour used as the final output of the ICD module is underlined.

Contour	$AP_{vol}$	$AP_{50}$	$AP_{70}$	FPS
$C_0$	49.5	61.2	31.9	51.5
$C_1$	56.1	65.6	49.2	48.4
$C_2$	58.5	66.3	53.8	45.1
$C_3$	59.3	66.5	54.4	37.9
$C_4$	59.6	66.6	54.7	34.6
$C_5$	59.7	66.6	54.7	30.5
$C_6$	59.7	66.7	54.8	28.8
$C_7$	59.7	66.7	54.9	26.1
$C_8$	59.7	66.7	54.9	23.6
$C_M$	<b>60.0</b>	<b>66.8</b>	<b>55.3</b>	24.6

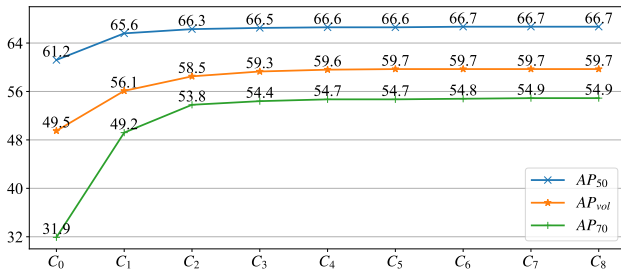


Fig. 7. Performance plot of the selected iterations during inference on the SBD val set [30].  $C_0$  is output initial contour of the ICG module.

## 4.2 Implementation Details

By default, we set the vertex number  $N_v = 128$  to form an object contour. The downsampling ratio  $R$  and the channel dimension  $D$  for feature map  $F$  are set as 4 and 64, respectively. The channel dimension  $D_v$  of contour feature  $g_{k-1}$  is 66. The channel dimension of feature map  $F_0, F_1, F'_0$  in the MCR module are 32, 16, and 8, respectively. We set  $\lambda = 0.8$  and  $\alpha = 1$  in Equation (9) to calculate loss  $\mathcal{L}_{ICD}$ , respectively. During training, we set the iteration number  $K$  as 6 for the SBD [30], Cityscapes [31], COCO [32], and KINS [33] dataset. By default, the iteration number during the inference is the same as that for the training.

## 4.3 Ablation Study

In this section, we conduct ablations to verify the effectiveness of the main components in our proposed PolySnake, including the initial contour generation, the iterative contour deformation, and the multi-scale contour refinement. Following previous methods [21], [28], all the ablations are studied on the SBD [30] dataset with 20 semantic categories, which well evaluates the algorithm capability to handle various object shapes. Note that in the ablations, our baseline network does not include the multi-scale contour refinement module.

**Initial contour generation.** We first validate the learning of category-agnostic boundary map  $B$  for the contour initialization. As shown in Table 1, with the learning of boundary map  $B$ , the performance of contour  $C_0$  and  $C_K$  are both slightly improved. This is because the learning of category-agnostic boundary map  $B$  helps to extract a more fine-grained feature map  $F$ , which improves the perception of object contour.



Fig. 8. Example results of the whole contour deformation process on the SBD val set [30]. PolySnake progressively refines the contour. The contour finally converges to a stable position, which tightly encloses the object instance. Zoom in for a better view.

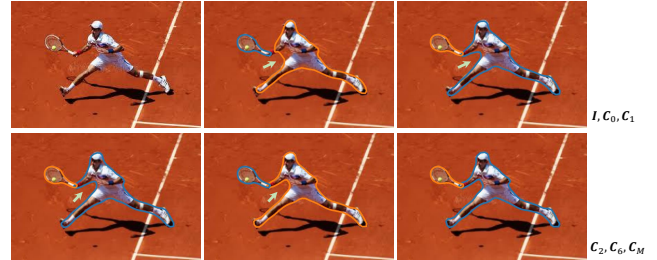


Fig. 9. Example results of the contour deformation process on the COCO [32] dataset. PolySnake progressively refines the contour to tightly enclose the object instance. Zoom in for a better view.

Furthermore, we test the impact of the vertex number  $N_v$  to construct a contour. The default vertex number  $N_v$  of PolySnake is 128. We study the other settings of vertex number  $N_v$  as 64 and 192, respectively. The results are reported in Table 1, which reveals that 128 vertices are enough to represent the contour of an object instance. In contrast, sampling more vertices (192) leads to worse performance. A likely reason is that it is difficult for the current contour feature extraction module to obtain a strong representation from an overlong vertex sequence.

**Iterative contour deformation.** We first validate the contour feature extraction used to construct the contour-level representation  $g_k$  of the estimated contour  $C_k$ . Specifically, as shown in Table 2, we train a baseline model that directly feeds the sampled vertex feature  $f_{k-1}$  to the recurrent updater (see Fig. 3). In other words, the baseline model does not aggregate the feature of the sampled vertices. With the aggregated vertex feature  $g_{k-1}$ , the result shows a performance gain of 1.1  $AP_{vol}$ . This improvement could be ascribed to the fact that the aggregated feature  $g_{k-1}$  encodes stronger context information of the current contour  $C_{k-1}$ , which is differentiated and processed by the recurrent updater to estimate further refinement.

In the ICD module, the default update unit is the ConvGRU, to which an alternative is the ConvLSTM, a modified version of the standard LSTM [61]. As shown in Table 2, while the ConvLSTM shows comparable performance, the ConvGRU produces slightly higher efficiency and accuracy.

By default, our PolySnake shares the weights across the total  $K$  iterations. An alternative version is to learn each vertex feature aggregation module and vertex coordinate update module (see in Sec. 3.2) with a distinctive set of weights. In Table 2, with the unshared weights, the performances are slightly worse while



Fig. 10. Qualitative results of PolySnake on the SBD val set [30]. Our method can segment object instances correctly in most cases, even when they are in some complex backgrounds or the detected boxes can not cover the objects tightly. It is best viewed in color.

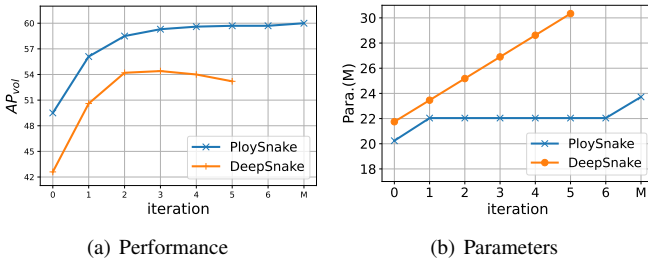


Fig. 11. Results of DeepSnake [21] and our PolySnake on the performance (left) and the parameter numbers (right) at different time steps on the SBD val set [30]. “0” denotes the initial contour for DeepSnake [21] and PolySnake. “M” represents the MCR module in PolySnake.

the parameter number significantly increases. For one thing, this can be attributed to the increased training difficulty of the large model size, which is verified in DeepSnake [21]. For another, our effective information transmission mechanism across iterations and the supervision at each iteration maintain the performance (see Table 2), different from DeepSnake [21].

We further compare our contour deformation pipeline with the classic DeepSnake [21]. In Fig. 11, we present the results of PolySnake and DeepSnake [21] in terms of the performance (left) and the parameter numbers (right) at different iterations on the SBD val set [30]. In DeepSnake [21], the iteration number is fixed as three by default. On the one hand, simply stacking more refinement modules ( $> 3$ ) introduces extra training; on the other hand, it does not necessarily improve the performance but the parameter number increases linearly. In contrast, for our PolySnake, the superior performance is obtained after convergence with only a lightweight model, indicating the stronger and stabler contour-deforming ability of our method.

During training, we propose a contour shape loss in Sec. 3.4. To validate its effectiveness, we evaluate the performance of our approach with and without it. As shown in Table 2, with the contour shape loss, a performance gain of 0.3  $AP_{vol}$  is achieved.

TABLE 4

Comparison of the  $AP_{vol}$ ,  $AP_{50}$ , and  $AP_{70}$  performances on the SBD val set [30]. “†” means that the multi-scale contour refinement module is used.

Method	Venue	$AP_{vol}$	$AP_{50}$	$AP_{70}$
MNC [62]	CVPR’16	-	63.5	41.5
FCIS [63]	CVPR’17	-	65.7	52.1
STS [23]	CVPR’17	29.0	30.0	6.5
ESE-20 [24]	ICCV’19	35.3	40.7	12.1
DeepSnake [21]	CVPR’20	54.4	62.1	48.3
DANCE [27]	WACV’21	56.2	63.6	50.4
EigenContours [46]	CVPR’22	-	56.5	-
E2EC [28]	CVPR’22	59.2	65.8	54.1
PolySnake	-	59.7	66.7	54.8
PolySnake <sup>†</sup>	-	<b>60.0</b>	<b>66.8</b>	<b>55.3</b>

We attribute this improvement to the fact that the proposed contour shape loss helps the learning of the object shape, which makes the estimated contour enclose the object tightly.

**Iterative and progressive mechanism.** To provide a more specific view of the iterative contour deformation process, we present the performance at the selected iteration in the inference stage. As shown in Table 3, the main contour deformation occurs in the top 3 iterations, while the later iterations further progressively fine-tune the result. We also present the performance plots in Fig. 7. As we can see, the results are getting better with iterations and the superior performance is obtained after convergence. These results verify the effectiveness of our method. In our final model, we set the iteration number  $K = 6$  to strike a balance between the accuracy and the running efficiency. Besides, the contour  $C_M$  achieves an improvement of 0.5  $AP_{70}$  compared with the contour  $C_6$ , which validates the effectiveness of the MCR module that further refines the contour at the full scale.

As shown in Fig. 8 and Fig. 9, we further visualize the contour deformation process with two samples. It can be seen that, during the contour deformation process, the predicted contours are progressively refined and finally converge to relatively steady positions enclosing the object tightly.



Fig. 12. Qualitative results of PolySnake on the Cityscapes test set [31]. Our method is able to correctly segment objects in most cases, even when they are in complex street scenes. It is best viewed in color.

TABLE 5

Performance comparison with other instance segmentation methods on the COCO val and COCO test-dev set [32]. “†” means that the multi-scale contour refinement module is added.

Method	Venue	Backbone	AP (val)	AP (test-dev)
ESE-Seg [24]	ICCV'19	Dark-53	21.6	-
YOLACT [36]	ICCV'19	R-50-FPN	-	28.2
YOLACT++ [64]	TPAMI'20	R-50-FPN	-	34.1
CenterMask [65]	CVPR'20	R-50-FPN	-	32.9
PolarMask [19]	CVPR'20	R-50-FPN	-	32.1
PolarMask++ [20]	TPAMI'21	R-101-FPN	-	33.8
DeepSnake [21]	CVPR'20	DLA-34	30.5	30.3
E2EC [28]	CVPR'22	DLA-34	33.6	33.8
PolySnake	-	DLA-34	34.4	34.5
PolySnake <sup>†</sup>	-	DLA-34	<b>34.8</b>	<b>34.9</b>

TABLE 6

Performance comparison on the KINS test set [33]. “\*\*\*” denotes with ASN proposed in [66]. “†” means that the multi-scale contour refinement module is added.

Method	Venue	AP
MNC [62]	CVPR'16	18.5
FCIS [63]	CVPR'17	23.5
ORCAN [67]	WACV'19	29.0
Mask R-CNN [9]	ICCV'17	30.0
Mask R-CNN * [66]	CVPR'19	31.1
PANet [12]	CVPR'18	30.4
PANet * [66]	CVPR'19	32.2
VRS&SP [68]	AAAI'21	32.1
ARCNN [69]	AI'22	32.9
DeepSnake [21]	CVPR'20	31.3
E2EC [28]	CVPR'22	34.0
PolySnake	-	35.0
PolySnake <sup>†</sup>	-	<b>35.2</b>

#### 4.4 Comparison with State-of-the-art Methods

**Performance on SBD.** PolySnake is implemented in Pytorch [76]. During training, we train the ICG and ICD modules end-to-end for 200 epochs. Then, we freeze their weights and train the MCR module for 50 epochs. The batch size is 40 for both training stages and we use Adam [77] as the optimizer. We use 4 and 2 RTX 2080Ti GPUs for the two training stages, respectively. The learning rate starts from  $1e-4$  and then decays based on the StepLR strategy. The network is trained and tested at a single scale of  $512 \times 512$ , following [21], [28], following DeepSnake [21].

In Table 4, we compare the proposed PolySnake with other contour-based methods [21], [23], [24], [27], [28], [46] on the SBD val set [30]. Our approach achieves 60.0  $AP_{vol}$  when the multi-scale contour refinement strategy is adopted. Compared with the classic DeepSnake [21], PolySnake yields 5.6  $AP_{vol}$ , 4.7  $AP_{50}$ , and 7.0  $AP_{70}$  improvements. Besides, PolySnake outperforms the recent state-of-the-art method E2EC [28] by 0.8  $AP_{vol}$ , 1.0  $AP_{50}$ ,

and 1.2  $AP_{70}$ . We present some qualitative segmentation results of our method in Fig. 10.

**Performance on COCO.** For the challenging COCO [32] dataset, we train the ICG and ICD modules following the strategy of E2EC [28]. Then, we freeze them and train the MCR module for another 50 epochs with the same strategy as the SBD [30] dataset. The network is trained at a single image scale of  $512 \times 512$  on 2 RTX 3090Ti GPUs. For the evaluation, we select a model that performs best on the validation set.

As shown in Table 5, our PolySnake achieves 34.8 and 34.9 AP on the COCO val and test-dev set, respectively. We outperform the classic DeepSnake [21] by 4.3 and 4.6 AP on the val and test-dev set, respectively. Besides, compared with the recent state-of-the-art method E2EC [28], we achieve a 1.2 and 1.1 AP improvement on the val and test-dev set, respectively.



TABLE 7

Comparison results on the Cityscapes val (“AP [val]” column) and test (remaining columns) sets [31]. Using only fine training data, PolySnake achieves superior performance on both the val and test sets. The inference time of method [21], [27], [28] and PolySnake are measured on a single RTX 2080Ti GPU, while we report the results of the other methods from their original papers. “†” means that the multi-scale contour refinement module is added.

Method	Training data	FPS	AP [val]	AP	AP <sub>50</sub>	person	rider	car	truck	bus	train	mcycle	bicycle
SGN [70]	fine + coarse	0.6	29.2	25.0	44.9	21.8	20.1	39.4	24.8	33.2	30.8	17.7	12.4
Mask R-CNN [9]	fine	2.2	31.5	26.2	49.9	30.5	23.7	46.9	22.8	32.2	18.6	19.1	16.0
GMIS [71]	fine + coarse	-	-	27.6	49.6	29.3	24.1	42.7	25.4	37.2	<b>32.9</b>	17.6	11.9
Spatial [72]	fine	11	-	27.6	50.9	34.5	26.1	52.4	21.7	31.2	16.4	20.1	18.9
PANet [12]	fine	<1	36.5	31.8	57.1	36.8	30.4	54.8	27.0	36.3	25.5	22.6	<b>20.8</b>
UPNet [73]	fine + COCO	4.4	37.8	33.0	59.6	35.9	27.4	51.8	31.7	43.0	31.3	<b>23.7</b>	19.0
SSAP [74]	fine	-	37.3	32.7	51.8	35.4	25.5	55.9	<b>33.2</b>	<b>43.9</b>	31.9	19.5	16.2
PolygonRNN++ [75]	fine	-	-	25.5	45.5	29.4	21.8	48.3	21.1	32.3	23.7	13.6	13.6
DeepSnake [21]	fine	4.6	37.4	31.7	58.4	37.2	27.0	56.0	29.5	40.5	28.2	19.0	16.4
DANCE [27]	fine	6.3	36.7	31.2	57.7	38.1	27.3	54.0	27.5	37.4	27.7	21.6	16.2
E2EC [28]	fine	4.9	39.0	32.9	59.2	39.0	27.8	56.0	28.5	41.2	29.1	21.3	19.6
PolySnake	fine	4.8	39.8	34.3	61.0	41.3	31.8	58.4	31.9	42.4	28.6	22.4	17.9
PolySnake <sup>†</sup>	fine	4.2	<b>40.2</b>	<b>34.6</b>	<b>61.2</b>	<b>42.2</b>	<b>32.8</b>	<b>59.2</b>	32.0	42.5	27.4	22.6	18.4



Fig. 13. Qualitative results of PolySnake on the KINS test set [33]. The top and bottom rows are the input images and their segmentation results, respectively. PolySnake can correctly segment objects with occluded parts in complex scenes. It is best viewed in color.

**Performance on Cityscapes.** As suggested in DeepSnake [21], we apply the component detection strategy [9] to handle the fragmented instances, which are frequently occurred in the dataset. We train the ICG and ICD modules end-to-end for 200 epochs with 16 images per batch on 4 RTX 2080Ti GPUs. Then, their weights are frozen and we train the MCR module for 50 epochs. The Adam optimizer [77] is used, and the learning rate schedule is the same as that for the SBD [30] dataset. We choose the model performing best on the validation set and the evaluation is conducted at a single resolution of  $1216 \times 2432$ , following DeepSnake [21].

As shown in Table 7, we compare our PolySnake with other state-of-the-art methods on the Cityscapes validation and test sets [31]. Using only the fine annotations, our approach achieves superior performances on both the validation and test sets. We outperform DeepSnake [21] by 3.5 AP and 3.4 AP on the validation set and test set, respectively. Compared with recent state-of-the-art E2EC [28], PolySnake achieves a 1.2 AP and 1.7 AP improvement on the validation and test set, respectively. We present some segmentation results in Fig. 12.

**Performance on KINS.** The KINS [33] dataset is used for amodal instance segmentation [59], and is annotated with inference completion information for the occluded parts of the instances. We first train the ICG and ICD modules for 150 epochs with the Adam optimizer [77]. The learning rate starts from  $1e - 4$  and is decayed by a factor of 0.5 at 80 and 120 epochs. Then, we freeze their weights and train the MCR module for another 50 epochs as the setting for the SBD [30] dataset. Following the classic DeepSnake [21], the models are trained and tested at a



Fig. 14. Failure cases of PolySnake. Top: if an initial contour does not involve a specific instance, the segmentation fails. Bottom: for instance with complex outlines, the obtained contour is not accurate enough.

single resolution of  $512 \times 512$  and  $768 \times 2496$ , respectively.

As shown in Table 6, the MCR module improves the performance from 35.0 AP to 35.2 AP. We note that the improvement is somewhat marginal. A likely reason is that the sampled vertex feature at the occluded parts can not provide the clues for further accurate refinement, different from the other three datasets [30], [31], [32]. Besides, our PolySnake outperforms DeepSnake [21] and E2EC [28] by 3.9 and 1.2 AP, respectively. We present some segmentation results in Fig. 13. It can be seen that the proposed

PolySnake can correctly segment objects with occluded parts to each other in complex urban scenes.

#### 4.5 Limitation Discussion

In this section, we discuss the limitation of our method with some typical cases. Similar to DeepSnake [21], our method also follows the paradigm of “Detect then Segment”. In other words, the proposed PolySnake requires the detection of an object instance first to initialize a contour for further progressive deformations. Note that such a contour deformation mechanism can tolerate the detection flaws to a certain extent, such as the inaccurate prediction of the center of an object. However, once the predicted center and its formed initial contour do not involve a specific object instance (see Fig. 14 top), the following segmentation process is senseless. This issue can be relieved by a powerful object detector. Besides, for some object instances with complex shapes, our method still can not obtain an accurate boundary prediction (see Fig. 14 bottom). A likely solution could be extracting a semantically stronger representation of an object contour.

### 5 CONCLUSION

In this work, we present PolySnake, an effective deep network architecture for contour-based instance segmentation. PolySnake simultaneously introduces the iterative and progressive learning mechanisms to facilitate the learning of contour estimation. By developing a recurrent architecture, PolySnake maintains a single estimation of a contour for each object instance and progressively updates it toward the object boundary. Through the iterative refinement, the contour finally progressively converges to a stable status that tightly encloses the object instance. Extensive experiments on the several prevalent benchmark datasets reveal the merits and superiority of our PolySnake over the existing advanced solutions. For future research, we will explore improving the state-of-the-art instance segmentation methods through effective integration with PolySnake. Moreover, it is significant to excavate our idea on other polygon or curve estimation problems in computer vision.

### REFERENCES

- [1] W.-C. Ma, S. Wang, R. Hu, Y. Xiong, and R. Urtasun, “Deep rigid instance scene flow,” in *Proceedings of the IEEE Conference on Computer Vision and Pattern Recognition*, 2019, pp. 3614–3622. 1
- [2] S. Grigorescu, B. Trasnea, T. Cocias, and G. Macesanu, “A survey of deep learning techniques for autonomous driving,” *Journal of Field Robotics*, vol. 37, no. 3, pp. 362–386, 2020. 1
- [3] H. A. Alhajja, S. K. Mustikovela, L. Mescheder, A. Geiger, and C. Rother, “Augmented reality meets deep learning for car instance segmentation in urban scenes,” in *Proceedings of the British machine vision conference*, vol. 1, 2017, p. 2. 1
- [4] H. Abu Alhajja, S. K. Mustikovela, L. Mescheder, A. Geiger, and C. Rother, “Augmented reality meets computer vision: Efficient data generation for urban driving scenes,” *International Journal of Computer Vision*, vol. 126, no. 9, pp. 961–972, 2018. 1
- [5] N. Fazeli, M. Oller, J. Wu, Z. Wu, J. B. Tenenbaum, and A. Rodriguez, “See, feel, act: Hierarchical learning for complex manipulation skills with multisensory fusion,” *Science Robotics*, vol. 4, no. 26, 2019. 1
- [6] K. Kleeburger, R. Bormann, W. Kraus, and M. F. Huber, “A survey on learning-based robotic grasping,” *Current Robotics Reports*, vol. 1, no. 4, pp. 239–249, 2020. 1
- [7] D. Li, Y. Li, Q. Xie, Y. Wu, Z. Yu, and J. Wang, “Tiny defect detection in high-resolution aero-engine blade images via a coarse-to-fine framework,” *IEEE Transactions on Instrumentation and Measurement*, vol. 70, pp. 1–12, 2021. 1
- [8] Q. Lin, J. Zhou, Q. Ma, Y. Ma, L. Kang, and J. Wang, “EMRA-Net: A pixel-wise network fusing local and global features for tiny and low-contrast surface defect detection,” *IEEE Transactions on Instrumentation and Measurement*, vol. 71, pp. 1–14, 2022. 1
- [9] K. He, G. Gkioxari, P. Dollár, and R. Girshick, “Mask R-CNN,” in *Proceedings of the IEEE International Conference on Computer Vision*, 2017, pp. 2961–2969. 1, 2, 8, 9
- [10] K. Chen, J. Pang, J. Wang, Y. Xiong, X. Li, S. Sun, W. Feng, Z. Liu, J. Shi, W. Ouyang *et al.*, “Hybrid task cascade for instance segmentation,” in *Proceedings of the IEEE Conference on Computer Vision and Pattern Recognition*, 2019, pp. 4974–4983. 1, 2
- [11] Z. Huang, L. Huang, Y. Gong, C. Huang, and X. Wang, “Mask Scoring R-CNN,” in *Proceedings of the IEEE Conference on Computer Vision and Pattern Recognition*, 2019. 1, 2
- [12] S. Liu, L. Qi, H. Qin, J. Shi, and J. Jia, “Path aggregation network for instance segmentation,” in *Proceedings of the IEEE Conference on Computer Vision and Pattern Recognition*, 2018, pp. 8759–8768. 1, 2, 8, 9
- [13] X. Shen, J. Yang, C. Wei, B. Deng, J. Huang, X.-S. Hua, X. Cheng, and K. Liang, “DCT-Mask: Discrete cosine transform mask representation for instance segmentation,” in *Proceedings of the IEEE Conference on Computer Vision and Pattern Recognition*, 2021, pp. 8720–8729. 1, 2
- [14] G. Zhang, X. Lu, J. Tan, J. Li, Z. Zhang, Q. Li, and X. Hu, “RefineMask: Towards high-quality instance segmentation with fine-grained features,” in *Proceedings of the IEEE Conference on Computer Vision and Pattern Recognition*, 2021, pp. 6861–6869. 1, 2
- [15] M. Hu, Y. Li, L. Fang, and S. Wang, “A2-FPN: Attention aggregation based feature pyramid network for instance segmentation,” in *Proceedings of the IEEE Conference on Computer Vision and Pattern Recognition*, 2021, pp. 15 343–15 352. 1, 2
- [16] C. Tang, H. Chen, X. Li, J. Li, Z. Zhang, and X. Hu, “Look closer to segment better: Boundary patch refinement for instance segmentation,” in *Proceedings of the IEEE Conference on Computer Vision and Pattern Recognition*, 2021, pp. 13 926–13 935. 1, 2
- [17] S. Minaee, Y. Y. Boykov, F. Porikli, A. J. Plaza, N. Kehtarnavaz, and D. Terzopoulos, “Image segmentation using deep learning: A survey,” *IEEE Transactions on Pattern Analysis and Machine Intelligence*, 2021. 1
- [18] E. Shelhamer, J. Long, and T. Darrell, “Fully convolutional networks for semantic segmentation,” *IEEE Transactions on Pattern Analysis and Machine Intelligence*, vol. 39, no. 4, pp. 640–651, 2017. 1
- [19] E. Xie, P. Sun, X. Song, W. Wang, X. Liu, D. Liang, C. Shen, and P. Luo, “PolarMask: Single shot instance segmentation with polar representation,” in *Proceedings of the IEEE Conference on Computer Vision and Pattern Recognition*, 2020. 1, 2, 8
- [20] E. Xie, W. Wang, M. Ding, R. Zhang, and P. Luo, “PolarMask++: Enhanced polar representation for single-shot instance segmentation and beyond,” *IEEE Transactions on Pattern Analysis and Machine Intelligence*, 2021. 1, 2, 8
- [21] S. Peng, W. Jiang, H. Pi, X. Li, H. Bao, and X. Zhou, “Deep snake for real-time instance segmentation,” in *Proceedings of the IEEE Conference on Computer Vision and Pattern Recognition*, 2020, pp. 8533–8542. 1, 2, 3, 4, 6, 7, 8, 9, 10
- [22] M. Kass, A. Witkin, and D. Terzopoulos, “Snakes: Active contour models,” *International Journal of Computer Vision*, vol. 1, no. 4, pp. 321–331, 1988. 1, 2, 3
- [23] S. Jetley, M. Sapienza, S. Golodetz, and P. H. Torr, “Straight to shapes: Real-time detection of encoded shapes,” in *Proceedings of the IEEE Conference on Computer Vision and Pattern Recognition*, 2017, pp. 6550–6559. 1, 7, 8
- [24] W. Xu, H. Wang, F. Qi, and C. Lu, “Explicit shape encoding for real-time instance segmentation,” in *Proceedings of the IEEE International Conference on Computer Vision*, 2019, pp. 5168–5177. 1, 2, 7, 8
- [25] J. Liang, N. Homayounfar, W.-C. Ma, Y. Xiong, R. Hu, and R. Urtasun, “PolyTransform: Deep polygon transformer for instance segmentation,” in *Proceedings of the IEEE Conference on Computer Vision and Pattern Recognition*, 2020, pp. 9131–9140. 1, 2
- [26] H. Ling, J. Gao, A. Kar, W. Chen, and S. Fidler, “Fast interactive object annotation with curve-GCN,” in *Proceedings of the IEEE Conference on Computer Vision and Pattern Recognition*, 2019. 1
- [27] Z. Liu, J. H. Liew, X. Chen, and J. Feng, “Dance: A deep attentive contour model for efficient instance segmentation,” in *Proceedings of the IEEE Winter Conference on Applications of Computer Vision*, 2021, pp. 345–354. 1, 2, 3, 4, 7, 8, 9
- [28] T. Zhang, S. Wei, and S. Ji, “E2EC: An end-to-end contour-based method for high-quality high-speed instance segmentation,” in *Proceedings of the IEEE Conference on Computer Vision and Pattern Recognition*, 2022, pp. 4443–4452. 1, 2, 3, 4, 6, 7, 8, 9
- [29] T. N. Kipf and M. Welling, “Semi-supervised classification with graph convolutional networks,” *arXiv preprint arXiv:1609.02907*, 2016. 1

- [30] B. Hariharan, P. Arbeláez, L. Bourdev, S. Maji, and J. Malik, "Semantic contours from inverse detectors," in *Proceedings of the IEEE International Conference on Computer Vision*, 2011, pp. 991–998. [2](#), [5](#), [6](#), [7](#), [8](#), [9](#)
- [31] M. Cordts, M. Omran, S. Ramos, T. Rehfeld, M. Enzweiler, R. Benenson, U. Franke, S. Roth, and B. Schiele, "The cityscapes dataset for semantic urban scene understanding," in *Proceedings of the IEEE Conference on Computer Vision and Pattern Recognition*, 2016, pp. 3213–3223. [2](#), [5](#), [6](#), [8](#), [9](#)
- [32] T.-Y. Lin, M. Maire, S. Belongie, J. Hays, P. Perona, D. Ramanan, P. Dollár, and C. L. Zitnick, "Microsoft COCO: Common objects in context," in *Proceedings of the European Conference on Computer Vision*, 2014, pp. 740–755. [2](#), [5](#), [6](#), [8](#), [9](#)
- [33] L. Qi, L. Jiang, S. Liu, X. Shen, and J. Jia, "Amodal instance segmentation with kins dataset," in *Proceedings of the IEEE Conference on Computer Vision and Pattern Recognition*, 2019, pp. 3014–3023. [2](#), [5](#), [6](#), [8](#), [9](#)
- [34] H. Ding, S. Qiao, A. Yuille, and W. Shen, "Deeply shape-guided cascade for instance segmentation," in *Proceedings of the IEEE Conference on Computer Vision and Pattern Recognition*, 2021, pp. 8278–8288. [2](#)
- [35] S. Ren, K. He, R. Girshick, and J. Sun, "Faster R-CNN: Towards real-time object detection with region proposal networks," *Advances in Neural Information Processing Systems*, vol. 28, 2015. [2](#), [5](#)
- [36] D. Bolya, C. Zhou, F. Xiao, and Y. J. Lee, "YOLOACT: Real-time instance segmentation," in *Proceedings of the IEEE International Conference on Computer Vision*, 2019, pp. 9157–9166. [2](#), [8](#)
- [37] H. Chen, K. Sun, Z. Tian, C. Shen, Y. Huang, and Y. Yan, "BlendMask: Top-down meets bottom-up for instance segmentation," in *Proceedings of the IEEE Conference on Computer Vision and Pattern Recognition*, 2020, pp. 8573–8581. [2](#)
- [38] Z. Tian, C. Shen, H. Chen, and T. He, "FCOS: Fully convolutional one-stage object detection," in *Proceedings of the IEEE International Conference on Computer Vision*, 2019, pp. 9627–9636. [2](#)
- [39] X. Wang, R. Zhang, T. Kong, L. Li, and C. Shen, "SOLOv2: Dynamic and fast instance segmentation," *arXiv preprint arXiv:2003.10152*, 2020. [2](#)
- [40] Z. Tian, C. Shen, and H. Chen, "Conditional convolutions for instance segmentation," in *Proceedings of the European Conference on Computer Vision*, 2020, pp. 282–298. [2](#)
- [41] W. Zhang, J. Pang, K. Chen, and C. C. Loy, "K-Net: Towards unified image segmentation," *arXiv preprint arXiv:2106.14855*, 2021. [2](#)
- [42] R. Guo, D. Niu, L. Qu, and Z. Li, "SOTR: Segmenting objects with transformers," in *Proceedings of the IEEE International Conference on Computer Vision*, 2021, pp. 7157–7166. [2](#)
- [43] J. C. Mason and D. C. Handscomb, *Chebyshev polynomials*, 2002. [2](#)
- [44] J. Redmon and A. Farhadi, "YOLOv3: An incremental improvement," *arXiv preprint arXiv:1804.02767*, 2018. [2](#)
- [45] T. Tang, W. Xu, R. Ye, Y.-F. Wang, and C. Lu, "ContourRender: Detecting arbitrary contour shape for instance segmentation in one pass," *arXiv preprint arXiv:2106.03382*, 2021. [2](#)
- [46] W. Park, D. Jin, and C.-S. Kim, "Eigencontours: Novel contour descriptors based on low-rank approximation," in *Proceedings of the IEEE Conference on Computer Vision and Pattern Recognition*, 2022, pp. 2667–2675. [2](#), [7](#), [8](#)
- [47] Z. Yang, Y. Xu, H. Xue, Z. Zhang, R. Urtasun, L. Wang, S. Lin, and H. Hu, "Dense reppoints: Representing visual objects with dense point sets," in *Proceedings of the European Conference on Computer Vision*, 2020, pp. 227–244. [2](#)
- [48] S. Suzuki *et al.*, "Topological structural analysis of digitized binary images by border following," *Computer vision, Graphics, and Image Processing*, vol. 30, no. 1, pp. 32–46, 1985. [2](#)
- [49] A. Vaswani, N. Shazeer, N. Parmar, J. Uszkoreit, L. Jones, A. N. Gomez, L. Kaiser, and I. Polosukhin, "Attention is all you need," *Advances in neural information processing systems*, vol. 30, 2017. [3](#)
- [50] Z. Tian, C. Shen, X. Wang, and H. Chen, "BoxInst: High-performance instance segmentation with box annotations," in *Proceedings of the IEEE Conference on Computer Vision and Pattern Recognition*, 2021, pp. 5443–5452. [3](#)
- [51] X. Zhou, D. Wang, and P. Krähenbühl, "Objects as points," *arXiv preprint arXiv:1904.07850*, 2019. [3](#), [4](#)
- [52] F. Yu, D. Wang, E. Shelhamer, and T. Darrell, "Deep layer aggregation," in *Proceedings of the IEEE Conference on Computer Vision and Pattern Recognition*, 2018, pp. 2403–2412. [3](#)
- [53] M. Jaderberg, K. Simonyan, A. Zisserman *et al.*, "Spatial transformer networks," *Advances in Advances in Neural Information Processing Systems*, vol. 28, 2015. [4](#)
- [54] P. Dai, S. Zhang, H. Zhang, and X. Cao, "Progressive contour regression for arbitrary-shape scene text detection," in *Proceedings of the IEEE Conference on Computer Vision and Pattern Recognition*, 2021, pp. 7393–7402. [4](#)
- [55] K. Cho, B. Van Merriënboer, D. Bahdanau, and Y. Bengio, "On the properties of neural machine translation: Encoder-decoder approaches," *arXiv preprint arXiv:1409.1259*, 2014. [4](#)
- [56] T.-Y. Lin, P. Dollár, R. Girshick, K. He, B. Hariharan, and S. Belongie, "Feature pyramid networks for object detection," in *Proceedings of the IEEE Conference on Computer Vision and Pattern Recognition*, 2017, pp. 2117–2125. [4](#)
- [57] M. Everingham, L. Van Gool, C. K. Williams, J. Winn, and A. Zisserman, "The pascal visual object classes (voc) challenge," *International Journal of Computer Vision*, vol. 88, no. 2, pp. 303–338, 2010. [5](#)
- [58] B. Hariharan, P. Arbeláez, R. Girshick, and J. Malik, "Simultaneous detection and segmentation," in *Proceedings of the European Conference on Computer Vision*, 2014, pp. 297–312. [5](#)
- [59] K. Li and J. Malik, "Amodal instance segmentation," in *Proceedings of the European Conference on Computer Vision*, 2016, pp. 677–693. [5](#), [9](#)
- [60] A. Geiger, P. Lenz, C. Stiller, and R. Urtasun, "Vision meets robotics: The kitti dataset," *The International Journal of Robotics Research*, vol. 32, no. 11, pp. 1231–1237, 2013. [5](#)
- [61] S. Hochreiter and J. Schmidhuber, "Long short-term memory," *Neural Computation*, vol. 9, no. 8, pp. 1735–1780, 1997. [6](#)
- [62] J. Dai, K. He, and J. Sun, "Instance-aware semantic segmentation via multi-task network cascades," in *Proceedings of the IEEE conference on Computer Vision and Pattern Recognition*, 2016, pp. 3150–3158. [7](#), [8](#)
- [63] Y. Li, H. Qi, J. Dai, X. Ji, and Y. Wei, "Fully convolutional instance-aware semantic segmentation," in *Proceedings of the IEEE Conference on Computer Vision and Pattern Recognition*, 2017, pp. 2359–2367. [7](#), [8](#)
- [64] D. Bolya, C. Zhou, F. Xiao, and Y. J. Lee, "YOLOACT++: Better real-time instance segmentation," *IEEE Transactions on Pattern Analysis and Machine Intelligence*, 2020. [8](#)
- [65] Y. Lee and J. Park, "CenterMask: Real-time anchor-free instance segmentation," in *Proceedings of the IEEE conference on Computer Vision and Pattern Recognition*, 2020, pp. 13 906–13 915. [8](#)
- [66] L. Qi, L. Jiang, S. Liu, X. Shen, and J. Jia, "Amodal instance segmentation with kins dataset," in *Proceedings of the IEEE Conference on Computer Vision and Pattern Recognition*, 2019. [8](#)
- [67] P. Follmann, R. König, P. Härtlinger, M. Klostermann, and T. Böttger, "Learning to see the invisible: End-to-end trainable amodal instance segmentation," in *Proceedings of the IEEE Winter Conference on Applications of Computer Vision*, 2019, pp. 1328–1336. [8](#)
- [68] Y. Xiao, Y. Xu, Z. Zhong, W. Luo, J. Li, and S. Gao, "Amodal segmentation based on visible region segmentation and shape prior," in *Proceedings of the AAAI Conference on Artificial Intelligence*, vol. 35, no. 4, 2021, pp. 2995–3003. [8](#)
- [69] X. Zeng, X. Liu, and J. Yin, "Amodal segmentation just like doing a jigsaw," *Applied Sciences*, vol. 12, no. 8, p. 4061, 2022. [8](#)
- [70] S. Liu, J. Jia, S. Fidler, and R. Urtasun, "SGN: Sequential grouping networks for instance segmentation," in *Proceedings of the IEEE International Conference on Computer Vision*, 2017, pp. 3496–3504. [9](#)
- [71] Y. Liu, S. Yang, B. Li, W. Zhou, J. Xu, H. Li, and Y. Lu, "Affinity derivation and graph merge for instance segmentation," in *Proceedings of the European Conference on Computer Vision*, 2018, pp. 686–703. [9](#)
- [72] D. Neven, B. D. Brabandere, M. Proesmans, and L. V. Gool, "Instance segmentation by jointly optimizing spatial embeddings and clustering bandwidth," in *Proceedings of the IEEE Conference on Computer Vision and Pattern Recognition*, 2019, pp. 8837–8845. [9](#)
- [73] Y. Xiong, R. Liao, H. Zhao, R. Hu, M. Bai, E. Yumer, and R. Urtasun, "UPSNet: A unified panoptic segmentation network," in *Proceedings of the IEEE Conference on Computer Vision and Pattern Recognition*, 2019, pp. 8818–8826. [9](#)
- [74] N. Gao, Y. Shan, Y. Wang, X. Zhao, Y. Yu, M. Yang, and K. Huang, "SSAP: Single-shot instance segmentation with affinity pyramid," in *Proceedings of the IEEE International Conference on Computer Vision*, 2019, pp. 642–651. [9](#)
- [75] D. Acuna, H. Ling, A. Kar, and S. Fidler, "Efficient interactive annotation of segmentation datasets with Polygon-RNN++," in *Proceedings of the IEEE Conference on Computer Vision and Pattern Recognition*, 2018, pp. 859–868. [9](#)
- [76] A. Paszke, S. Gross, S. Chintala, G. Chanan, E. Yang, Z. DeVito, Z. Lin, A. Desmaison, L. Antiga, and A. Lerer, "Automatic differentiation in pytorch," 2017. [8](#)
- [77] D. P. Kingma and J. Ba, "Adam: A method for stochastic optimization," *arXiv preprint arXiv:1412.6980*, 2014. [8](#), [9](#)